5.1. Introduction

Electronic devices with miniaturization, high-integration, intellectualization, and multifunctionalizations have garnered rising attention for dielectric capacitor applications, in line with the rapid development of the power electronics sector and capacitive storage technology [**1**–**6**]. Dielectric materials with colossal permittivity ($\varepsilon' \geq 10^3$) accompanied by relatively a low dielectric loss ($\tan \delta \leq 0.1$) are importantly needed to satisfy the above requirement. In this consideration, new high dielectric materials have been developed by researchers enormously essential for next-generation high-performance capacitive devices such as distributed power systems, 5G communications hybrid electric vehicles, and renewable energy storage applications [**4**, **7**]. $CaCu_3Ti_4O_{12}$(CCTO) has attracted much attention in particular over the past few years because of its interesting unusual physical properties. It exhibits extremely large ε' values over 10^4, insignificant temperature dependence on permittivity over the wide temperature range from 100 to 600 K, and frequency independence in a wide frequency range [**8**, **9**]. Although several methods have been employed for the fascinating dielectric properties with good thermal stability and low dielectric loss of CCTO ceramic to meet the requirements for practical applications [**10**–**12**]. The mystery of the origin of giant dielectric constant in CCTO ceramic has been explained in terms of internal barrier layer capacitor (IBLC) effects arising from interfacial polarization of n-type semiconducting grains across the insulating grain boundaries. These are especially diverse from that of a few different perovskite materials such as $Pb(Zr,Ti)O_3$ and $BaTiO_3$, where the main contributor of huge dielectric permittivity is typically due to the dipolar polarization in the ferroelectric state [**13**–**15**]. The presence of an electrically resistive barrier at the grain boundary, according to the IBLC model, restricts electron transport and

establishes a huge polarization from the gathered charges [**16**]. As a result, recognizing the electrical characteristics of the grain boundary is important to understanding the abnormally large dielectric constant of CCTO [**17**]. Most of the studies on grain boundaries of CCTO materials have been based on the using microcontact current–voltage (I-V) measurements and Kelvin probe force microscopy, S. Y. Chung [**18**] evidenced the assumption of insulator-semiconductor junction that support the IBLC model in which large potential barrier existed intrinsically at grain boundaries of CCTO. The electrical structure obtained because of the presence of semiconducting grains parted by insulating grain boundaries has dielectric relaxation spectra similar to the Debye relaxation process which is mostly owing to dipole relaxation [**19**]. Here are various phenomena that believed as the primary source of large dielectric behaviour of CCTO ceramics such as IBLC, Maxwell–Wagner polarization of electrode-sample interfaces, grain boundaries, phase boundaries, and domain boundaries [**20**, **21**]. Despite that, a second relaxation had only been observed in polycrystalline CCTO ceramics till now but S. Krohns and P. Lunkenheimer [**22**] were also found in CCTO single crystals. Moreover, the suggested nanoscale barrier layer capacitance (NBLC) model was established to confess differing interpretations on both intrinsic and extrinsic about the origins of unusually giant dielectric constants of CCTO in its numerous forms [**23**]. The essential relationship between dielectric permittivity, conductivity, and intrinsic point defects of CCTO has recently been proposed with the help of a new model of trapped electron relaxation of the Schottky barrier [**24**, **25**]. Various theoretical models have been widely accepted for the colossal dielectric permittivity but are still controversial.

In the last decades, many $ACu_3Ti_4O_{12}$ (A=Ca, Sr, $Bi_{2/3}$, $Bi_{1/2}Na_{1/2}$, $La_{2/3}$, etc.) types of oxides have been recognized which confirmed to reveal giant dielectric properties [**26**]. BCTO ($Bi_{2/3}Cu_3Ti_4O_{12}$) ceramic has a very similar structure to the structure of CCTO ceramic [**27**].

Z. Yang et al. synthesized the series of high density BCTO ceramics by sol–gel method which have outstanding colossal permittivity of approximately 2.2×10^4 at 1 kHz [**28**]. When it was prepared via the conventional solid-state method by L. Yang, then it has been observed that the colossal dielectric constant of ~3.3×10^5 [**15**]. P. Gautam et al. have also synthesized BCTO by semi wet route and observed a high dielectric constant of approximately 8×10^3 at 323 K and 1 kHz but the tangent loss (~10) of this ceramic was very high, making not more it suitable for practical application [**29**]. Therefore, further to see the effect of doping of metal ions in BCTO is necessary to have a better understanding of its physical properties. In the present work, the Gadolinium (Gd) doped BCTO ceramic i.e.; $Bi_{(2/3)-x}Gd_xCu_3Ti_4O_{12}$(x=0.05, 0.10, and 0.20) designated as BGCTO-0.05, BGCTO-0.1, and BGCTO-0.2 were successfully prepared by semi wet route at low sintering temperature with short duration is being reported. To the best of our knowledge, there are no reports on the preparation of Gd-doped BCTO ceramic using solid TiO_2 as a raw material in a non-aqueous solvent. The microstructure, crystalline structure, dielectric properties (the values of ε′ and tan δ), and electrical properties of the BGCTO-0.05, BGCTO-0.1, and BGCTO-0.2 ceramic were systematically investigated

5.2. Experimental

Analytical grade chemicals namely Bismuth nitrate $Bi(NO_3)_35H_2O$ (99% Merck, India), copper acetate $Cu(CH_3COO)_2H_2O$ (99% Merck, Gd_2O_3(99.9% Aldrich, India), titanium oxide TiO_2 (98.5% Merck, India) and citric acid (≥99% Merk Mumbai, India) were used for the preparation of $Bi_{(2/3)-x}Gd_xCu_3Ti_4O_{12}$(x= 0.05, 0.10 and 0.20) ceramic via semi wet route. In this method, all above mentioned chemicals were taken in their stoichiometry ratios and dissolved in the double distilled water in a beaker and a separate solution of citric acid per equivalent to metal ions was also added into the resulting solution. After that, the resulting

solution mixer was heated on a hot plate using a magnetic stirrer with constant stirring at 70–80 °C for 24 h–28 h to remove excess water. A blue gel was formed during the evaporation and dry powders of BGCTO were obtained after the complete combustion. A large number of gases are exhausted from BGCTO samples during the combustion process. Finally, dry powers were collected and grounded gently with the help of agate and mortar pestle and calcined in air at 800 °C for 6 h. Further, the resulting powders were mixed with 2–3 drops of polyvinyl alcohol (PVA) as a binder. The obtained BGCTO-0.05, BGCTO-0.1, and BGCTO-0.2 powders were shaped into pellets using formerly described procedures [**30**]. These disk-shaped bodies of BGCTO-0.05, BGCTO-0.1, and BGCTO-0.2 powders were sintered at 1173 K for 8 h in the air for different physio-chemical characterizations.

The crystalline phase of BGCTO-0.05, BGCTYO-0.1, and BGCTO-0.2 sintered ceramic was analyzed by X-ray diffractometry (MiniFlex2 goniometer, Rigaku, Tokyo, Japan) using Cu-Kα radiation (λ = 1.54 Å). The microstructure and chemical composition of the grains and grain boundaries of sintered materials were examined using a scanning electron microscope (ZEISS model, EVO-18 Germany) with an energy dispersive X-ray (EDX) analyzer (Oxford instrument; USA). The particle size of BGCTO ceramic with chemical compositions x = 0.05, 0.1, and 0.2 was measured by Bright-Field TEM images through transmission electron microscopy (TEM, FEI Tecnai-20G). The atomic force microscopy (NTEGRA Prima, Germany) was also used for the surface roughness. The oxidation states of the element present in the BGCTO ceramic were determined by X-ray photoelectron spectroscopy (XPS). The Silver-coated disk-shaped body was utilized for the determination of dielectric and impedance data of ceramics using the LCR meter (PSM 1735, Newton 4th Ltd, U.K).

5.3. Results and discussion

5.3.1. Microstructural studies

Figure **5.1**(a) reveals the XRD patterns of BGCTO-0.05, BGCTO-0.1, and BGCTO-0.2 ceramics sintered at 1173 K for 8h. The XRD patterns of these ceramics are perfectly indexed with the help of JCPDS card no. 46-0725 [**31**], which indicates single-phase formation of ceramics with body centered cubic structure. No other extra impurity phase was observed in the XRD pattern of all ceramics. From X-ray diffraction analysis, it is observed that BGCTO ceramic contained a single phase's cubic structure with the space group Im-3. The values of average crystallite size (D) for the BGCTO-0.05, BGCTO-0.1, and BGCTO-0.2 ceramics were calculated from the XRD data with the help of Debye– Scherrer's formula and found to be 56.81 nm, 54.26 nm, and 53.09 nm, respectively which implies that the value of average crystallite size decreases with an increasing gadolinium concentration. The decrease in the average value of D with increasing compositions of gadolinium may be attributed to the difference in ionic radius of Gd^{3+}(0.93 Å) and Bi^{3+}(1.03 Å).

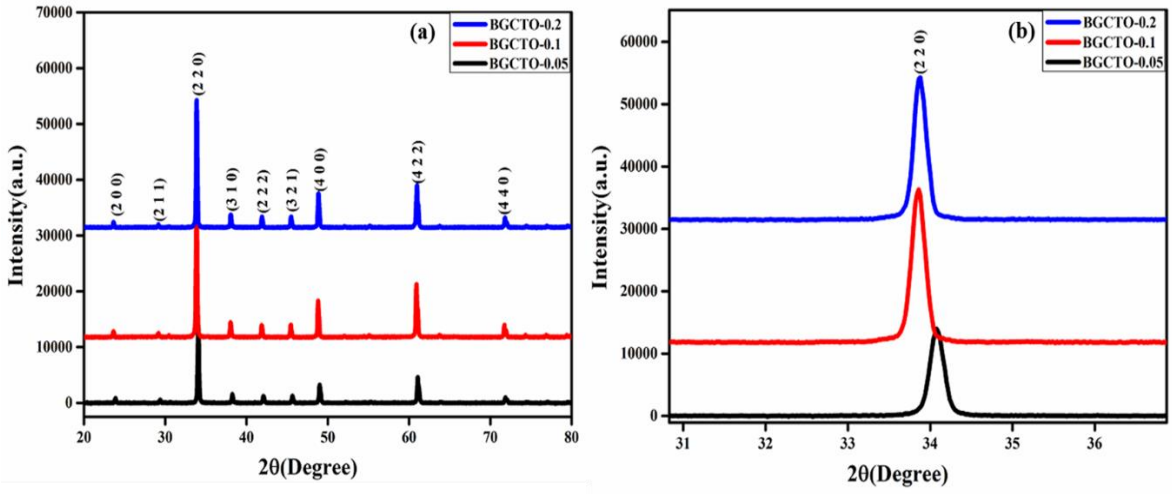

Fig. 5.1 (a**)** The XRD patterns and (b**)** enlargement view of most instance peaks of $Bi_{(2/3)-x}Gd_xCu_3Ti_4O_{12}$ (x = 0.05, 0.10 and 0.20) ceramics sintered at 1173 K for 8 h.

Rietveld refinement of XRD data was also carried out by using Fullprof software for phase confirmation and the change in the lattice parameters of the BGCTO-0.05, BGCTO-0.1, and BGCTO-0.2 ceramics, are shown in Figure **5.2**. The conditions regarding Rietveld refinement of BGCTO ceramic with few selected Gd concentrations are reported in Table 1. The linear interpolation method is used for the modeling of the background and on the other hand, pseudo-Voigt axial divergence symmetry function was also carried out for refinement of the peak shape of the XRD pattern. The refinement procedure also included variations in atomic locations; zero correction, unit cell parameters, half width parameters (U, V, and W), background, atomic occupancy, and scale factor. Further, the experimental data are assigned as a black line whereas the red line depicts the calculated pattern and the blue line shown in the figure represents the difference between the experimental and calculated pattern [**32**]. The position of Bragg is depicted by the pink vertical lines. The lower value of χ^2 and overlapping of the experimental and calculated pattern indicates the best fitting of XRD results. As the replacement content rises, the (220) peak in Figure **5.1**(b) shows a little peak displacement toward a higher diffraction angle, which was also the case when X. Huang et al.[**33**] reported a similar pattern. A small decrement in lattice parameters and unit cell volume is observed for the above ceramics which may be due to smaller ionic radii of Gd^{3+} (0.93 Å) than host site Bi^{2+} (1.03 Å) cation (table 1).

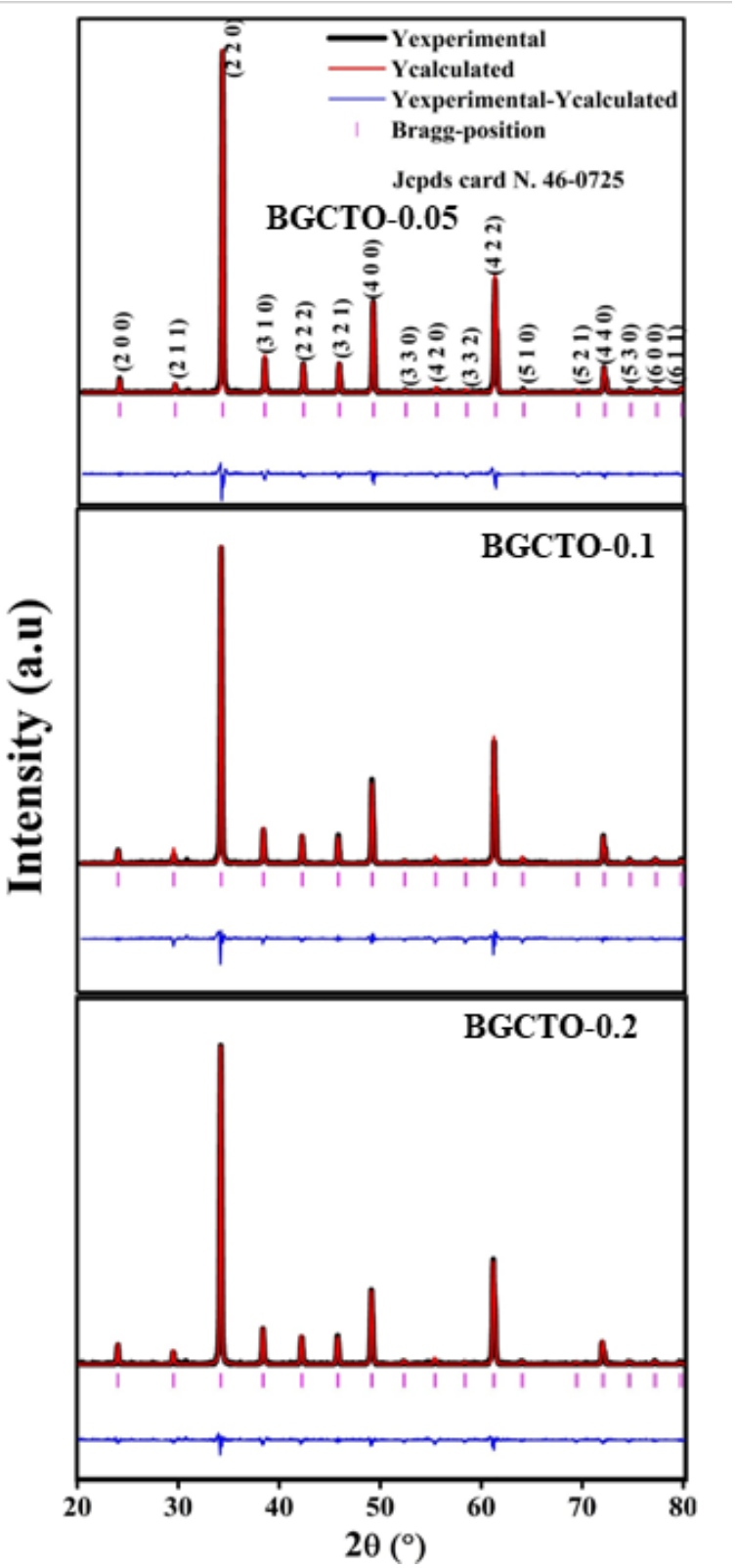

Fig. 5.2 Rietveld refinement of XRD profiles of the $Bi_{(2/3)-x}Gd_xCu_3Ti_4O_{12}$ (x=0.05, 0.10 and 0.20) ceramic

Table 5.1 Conditions for refinement, chi-square (χ^2), Phase, Crystallite size, reliability factor (R_p, R_{wp}, R_{exp}), Full-width at half maximum (FWHM) parameters, Bragg R-factor (%), RF-factor (%) and Lattice parameters for BGCTO-0.05, BGCTO-0.1 and BGCTO-0.2 ceramic.

Concentrations	0.05	0.1	0.2
λ (Å)	1.54046	1.54046	1.54046
Cycles of refinement	15	15	15
Step (°)	0.020	0.020	0.020
Profile function	P-voigt*Axial Divergence symmetry	P-voigt* Axial Divergence symmetry	P-voigt* Axial Divergence symmetry
χ^2	5.43	4.57	4.32
Phases	BCC	BCC	BCC
The space group of phase	lm-3	lm-3	lm-3
Crystallize size (nm)	56.81	54.26	53.09
R_p (%)	18.3	20.0	26.3
R_{wp} (%)	37.4	43.8	81.9
R_{exp} (%)	8.74	6.71	6.79
U	0.050312	0.035108	0.025407
V	-0.002948	-0.037701	-0.003736
W	0.023967	0.037616	0.021174
Bragg R-factor (%)	0.6742	2.202	1.141
RF-factor (%)	0.7436	1.886	1.287
a = b = c in Å	7.414230	7.400065	7.392699
Vcell ($Å^3$)	407.5662	405.2667	404.0257

Figure **5.3**(a, c, e) demonstrates the TEM images of BGCTO-0.05, BGCTO-0.1, and BGCTO-0.2 ceramics sintered at 1173 K for 8 h. The TEM result shows that the images of ceramics consist of polycrystalline with a cubical shape having particle sizes 90.85±5 nm, 75.35±5 nm,

and 72.43±5 nm, respectively measured on the scale of 200 nm. It was also observed from the figure of TEM images, the presence of dispersion of particles with some agglomeration of prepared materials. From the above measurements, it is observed that the size of the particle decreases with increasing gadolinium concentrations in BCTO. Figure **5.3**(b, d, f) represents the selected area electron diffraction pattern of BGCTO-0.05, BGCTO-0.1, and BGCTO-0.2 ceramics, respectively. The SEAD pattern shows the existence of a few rings with a bright spot which confirms the polycrystalline nature of ceramics.

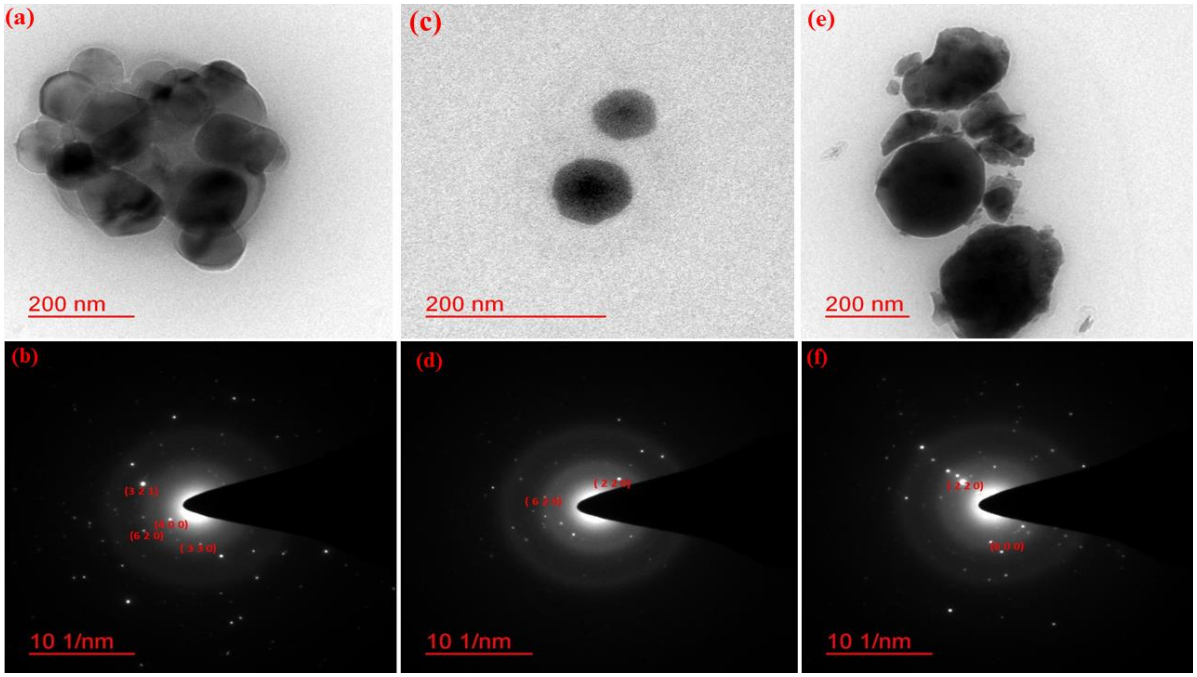

Fig. 5.3 Bright-field TEM images well as SAED patterns of (a, b) x=0.05, (c, d) x=0.1 and (e, f) x=0.2 for $Bi_{(2/3)-x}Gd_xCu_3Ti_4O_{12}$ (x = 0.05, 0.10 and 0.20) ceramics sintered at 1173 K for 8 h.

The microstructure of the BGCTO-0.1, and BGCTO-0.2 sintered ceramics (shown in Figure **5.4**(a-c)) were studied using an HR-SEM and the size of the grains seen in the SEM morphology was analyzed with the help of Image J software. From the figure of SEM images, fined microstructure with clear grain is observed in the case of BGCTO-0.05, BGCTO-0.1, which is separated by grain boundaries while a slight agglomeration was noticed in BGCTO-

0.2 ceramic. Further, some degree of porosity is also present in Gd-doped BCTO ceramic which may be due to an evolution of some significant gasses during the combustion of citrate–nitrate precursor gel [**34**]. The average grain size of the BGCTO-0.05, BGCTO-0.1 and BGCTO-0.2 sintered ceramics are 0.531 μm, 0.582 μm and 0.567 μm, respectively. Figure **5.4** (d-f) demonstrates the energy-dispersive X-ray (EDX) spectra of BGCTO-0.1, and BGCTO-0.2 ceramics sintered at 1173 K for 8 h which agree with the presence of Bi, Gd, Cu, Ti, and O elements.

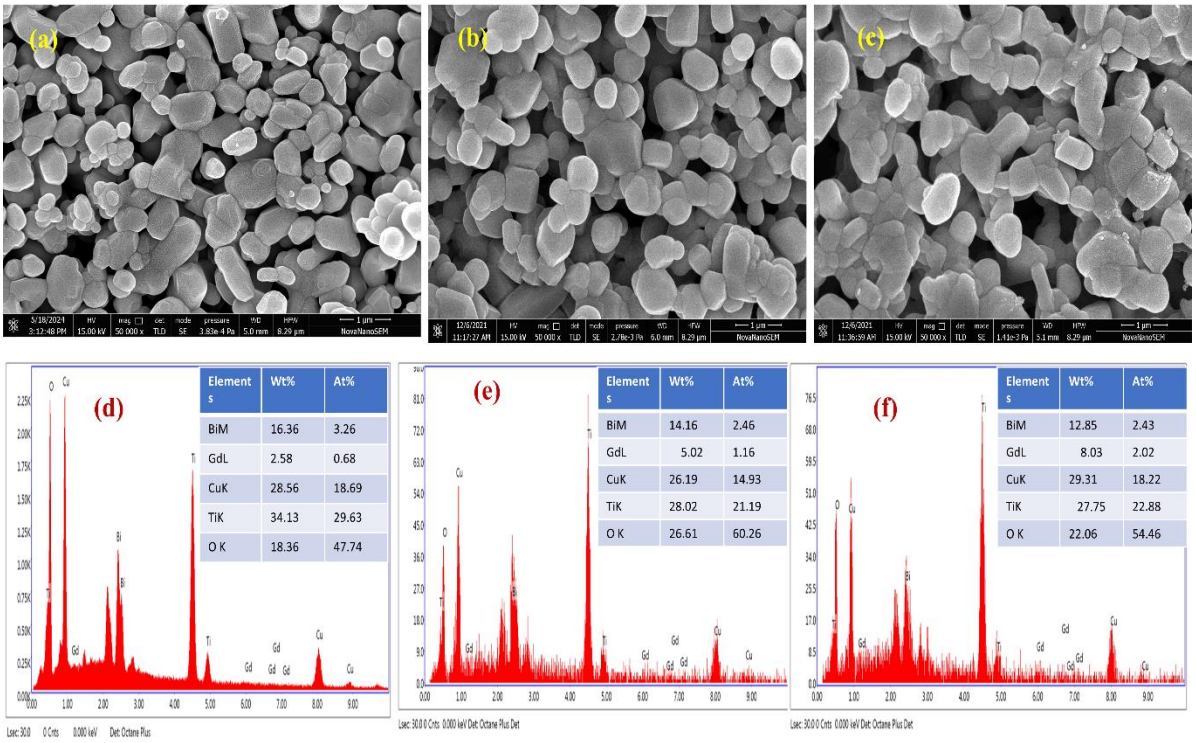

Fig. 5.4 (a-c) and (d-f), the FE-SEM images of the fractured surfaces and EDX images of $Bi_{(2/3)-x}Gd_xCu_3Ti_4O_{12}$ ceramics(x= 0.05, 0.10 and 0.20) sintered at 1173 K for 8 h.

Figure **5.5** reveals the microstructure of the fractured surface of BGCTO-0.2 sintered ceramic observed by AFM. It was observed from Figure **5** (a) that the existence of clear grains separated by grain boundaries with bimodal structure in the materials by two-dimensional (2D) AFM image. Figure **5.5** (b) shows the 3D image of ceramics where the maximum area

peak height (S_p), average roughness (S_a), and root mean square roughness (S_q)were found 1.417 µm, 0.314 µm, and 0.401µm, respectively on the scanned area of 20×20. The grain size of the BGCTO-0.2 ceramic was determined by histogram plots for 2D AFM images and is found to be in the range of 0.5 µm-1.2 µm, which is comparable to the SEM results as indicated in Fig. **5.5** (e).

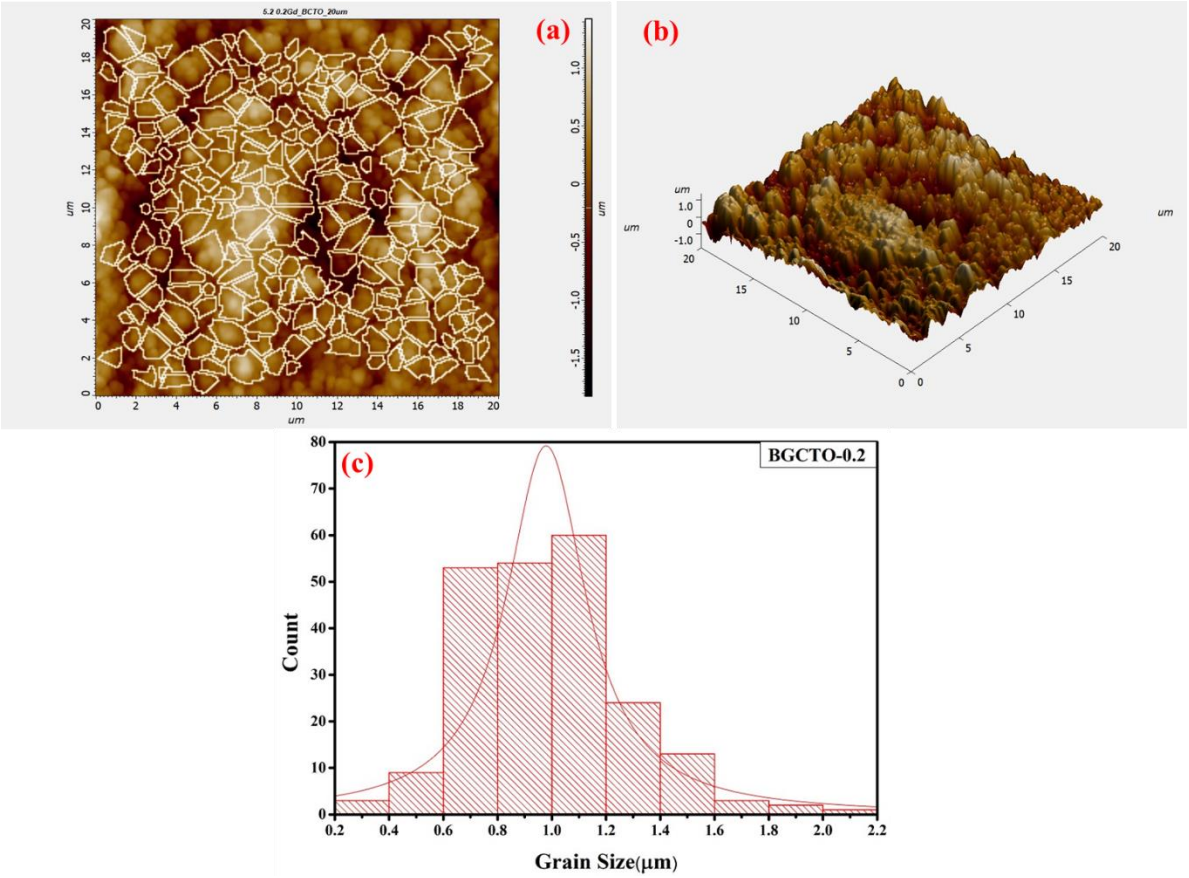

Fig. 5.5 AFM images of $Bi_{(2/3)-x}Gd_xCu_3Ti_4O_{12}$ ceramic with a composition of x = 0.2, (a) two-dimensional image for grain boundary, (b) three-dimensional image for surface roughness, (c) depth histogram graph.

High-**r**esolution X-ray photoelectron spectroscopy (XPS) analysis of BGCTO-0.2 ceramic has been investigated to confirm the chemical state of the element on the sample surface. Figure **5.6 (**a-e) reveals XPS spectra of the Bismuth (Bi), Gadolinium (Gd), Copper (Cu), Titanium (Ti), and Oxygen (O) elements for the BGCTO-0.2 ceramic. In this study, Carbon

1s was taken as a reference which has an assigned value of 284.6 eV to compensate for the surface of charge effects. Figure **5.6** (a) depicts the Bi 4f spectrum having two typical peaks for Bi 4f emerged at about 158.77 eV and 164.08 eV, respectively, corresponding to Bi $4f_{7/2}$ and Bi $4f_{5/2}$, suggesting the presence of bismuth as Bi^{3+} in BGCTO-0.2 [**35**]. The XPS spectrum of Gd 4d is shown in Figure **5.6** (b) that can be deconvoluted into three peaks centered at 141.01 eV, 142.99 eV, and 147.83 eV in which first two peaks corresponding to Gd $4d_{5/2}$ and later one corresponds to Gd $4d_{3/2}$ respectively, verifying the existence of Gd^{3+} valence state in the BGCTO-0.2 ceramic [**36**]. The XPS spectra of Cu2p display the two binding energies peak with satellite peaks as shown in Figure **5.6** (c). The binding energy peaks 933.79 eV and 953.71 eV correspond to Cu $2p_{3/2}$ and Cu $2p_{1/2}$ confirming the existence of the +2 oxidation state of Cu in the BGCTO-0.2 ceramic [**37**]. Figure **5.6** (d) demonstrates the XPS spectra of Ti 2p which show four peaks positioned at 458.02 eV, 463.91 eV, 459.05 eV, and 465.95 eV. The first two peaks correspond to the Ti 2p doublet namely Ti $2p_{3/2}$ and Ti $2p_{1/2}$ confirming the presence of the +4 oxidation state of Ti ion and the later two peaks indicate the existence of Ti ion in the +3 oxidation state which may be due to the existence of oxygen vacancy during sintering at high temperature [**38**]. The O 1s XPS spectrum (Figure **5.6** (e)) displays the two peaks placed at 529.57 eV and 530.91 eV could be attributed to oxygen lattice i.e., oxygen–metal bond and oxygen vacancy (V_o), respectively [**39**].

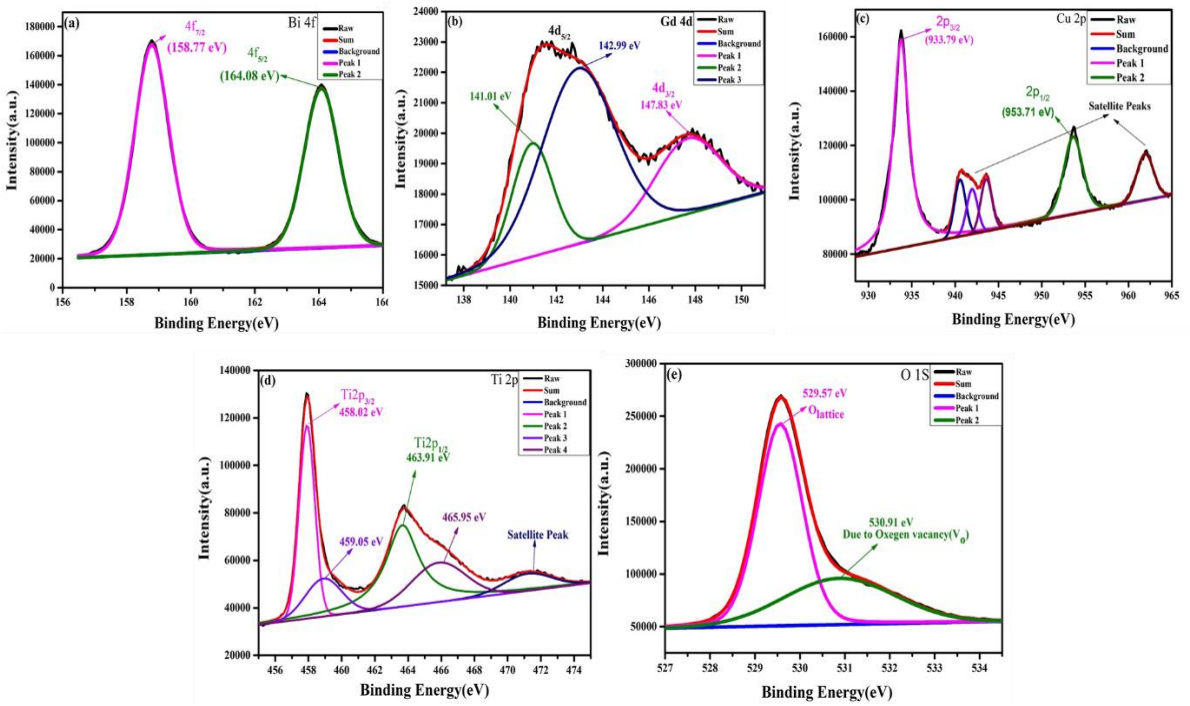

Fig. 5.6 XPS spectra of (a) Bi; (b) Gd; (c) Cu; (d) Ti; (e) O of $Bi_{(2/3)-x}Gd_xCu_3Ti_4O_{12}$(x=0.2) ceramic sintered at 1173 K for 8 h

5.3.2. Dielectric Studies

Figure **5.7** shows the frequency dependent dielectric constant (ε′) and tangent loss (tan δ) of BGCTO-0.05, BGCTO-0.1, and BGCTO-0.2 ceramics sintered at a few selected temperatures. In Figure **5.7** (a), we observed that the value of ε′ decreases with increasing frequency and is drastically reduced in the higher frequency region of 10^3-10^7 Hz. The presence of high ε′ in the lower frequency region may be attributed to the influence of interfacial polarization and barrier layer formation at grain-grain boundaries. The values of the dielectric constant of BGCTO-0.05, BGCTO-0.1, and BGCTO-0.2 at room temperature (309 K) and 1 kHz are pointed out as 99.34, 160.12, and 175. 25 respectively. Figure **5.7** (b) reveals the dielectric loss (tan δ) of BGCO-0.05, BGCTO-0.1, and BGCTO-0.2 sintered ceramics at fixed temperatures as a function of frequency. The value of tan δ is found to be

from the plots and is 0.08, 0.145, and 0.22 respectively at 309 K and 1 kHz, which is much lower than the undoped BCTO. The above results show that the value of tan δ declines with rising frequency. The values of the dielectric constant and dielectric loss of the above ceramics at fixed frequency are also summarized in Table **2**

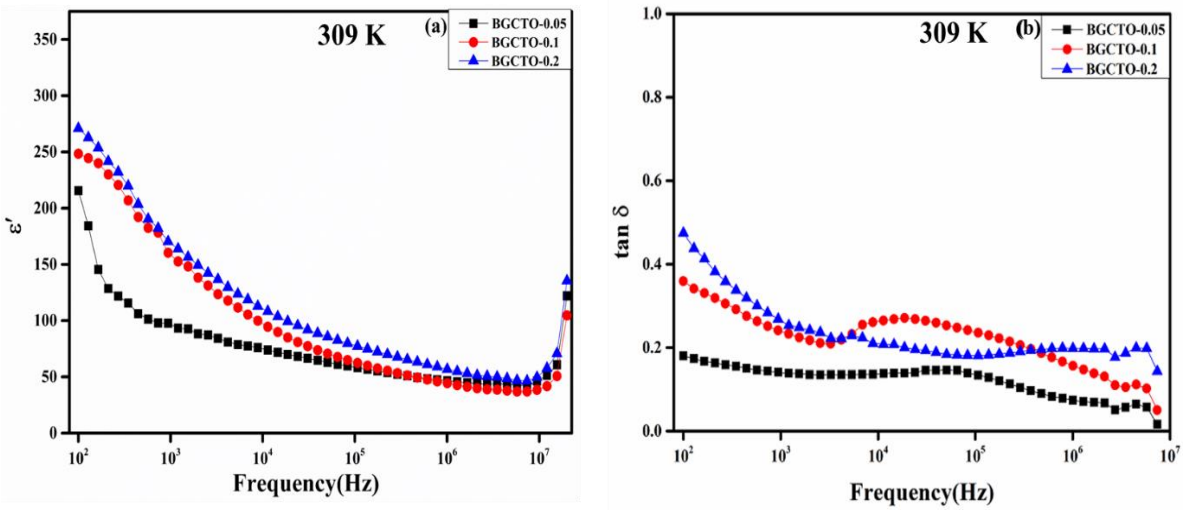

Fig. 5.7 (a) and (b) the frequency dependence of ε′ and tan δ of $Bi_{(2/3)-x}Gd_xCu_3Ti_4O_{12}$ (x = 0.05, 0.10 and 0.20) ceramics sintered at 1173 K for 8 h.

Table 5.2 Representing comparative table of the obtained dielectric constant and dielectric loss between the current work and the reported work

Samples	Dielectric Constant (ε′) at 1 kHz	Tangent Loss (tan δ) at 1 kHz	Reference
BCTO	8000 (at 323 K)	9.89 (at 323 K)	P. Gautam et al 26.6 (2016): 567-571 Prog. Nat. Sci. Mater. Int.[**29**]
BGCTO-0.05	99.34 (at 309 K)	0.08 (at 309 K)	
BGCTO-0.10	160.12 (at 309 K)	0.15 (at 309 K)	
BGCTO-0.20	175.25 (at 309 K)	0.22 (at 309 K)	

The complex impedance spectroscopy (CIS) techniques or Cole-Cole plot was applied to analyses impedance of the electrodes, grains and grain boundaries in ceramics. The

capacitance along with resistance associated with the grains and grain boundaries are estimated using CIS. A Cole-Cole plot is comprised of a couple of semicircles. One is due to grain boundary contribution in the lower frequency region and the other is due to grain contribution in the higher frequency zone. Figure **5.8** (b) shows the Cole-Cole plot of BGCTO-0.05, BGCTO-0.1, and BGCTO-0.2 sintered ceramics at various temperatures (309 K -509 K). The figure reveals the existence of a semicircular arc which is evidently due to the grain boundaries contribution at a lower frequency region. The inset of Figure **5.8** (b) at room temperature exhibits the data in higher frequency and it was observed by the extrapolation impedance plot that indicates some values on the Z' axis, the intercept does not find to pass through the origin which explained another semicircular arc at a higher frequency region that is beyond our measurements the contribution of grain resistance. The non-zero intercepts on the Z' axis give the resistance of grains (R_g) while the semicircular arc obtained in the lower frequency region is the contribution of gains boundaries resistance (R_{gb}). The complex impedance (Z^*) is the function of real (Z') and imaginary (Z'') impedance offered by grains-grain boundaries which can be expressed by the following equation [40]. The arc for grains in the high frequency range is suppressed by the significant value of grain boundary resistance that is commonly observed for the IBLC mechanism which is a characteristic of semiconducting grains with insulating grain boundaries [**41**]. It is clear from the figure that the value of grains and grain boundary resistance declines with the rise in concentration of Gd^{3+}. The values of grain and grain boundary resistance of BGCTO-0.05, BGCTO-0.1, and BGCTO-0.2 at room temperature (309 K) are measured from the plot and it is observed to decrease with a rise in compositions. The values of grain resistance for the above BGCTO ceramic are observed at 1216 Ω,1195 Ω, and 1156 Ω while grain boundary resistance was found to be $3.65\times10^7\Omega$, $3.5\times10^7\Omega$, and $2.31\times 10^7\Omega$ respectively.

Figure **5.8** (a) demonstrates the frequency-dependent imaginary part of impedance (Z″) at a few selected temperatures of BGCTO-0.05, BGCTO-0.1, and BCGTO-0.2 sintered ceramics. Z″ drops with rising frequency and merges in the higher frequency region, as shown in the graph. The relaxation peaks observed at lower frequency regions and suppression as well as shifting of relaxation peaks occurring at higher frequency regions support the existence of the temperature-dependent thermally assisted ionic phenomenon in Gd-doped BCTO ceramic [**42**].

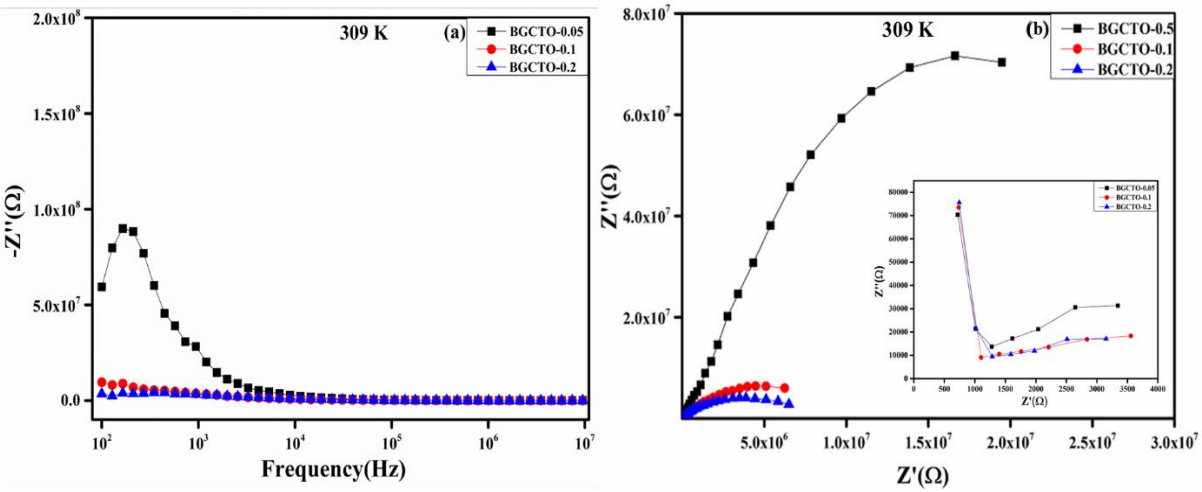

Fig. 5.8 (a) and (b), frequency dependence of imaginary part of impedance (Z″) and the complex impedance plot for $Bi_{(2/3)-x}Gd_xCu_3Ti_4O_{12}$ (x = 0.05, 0.10 and 0.20) ceramics sintered at 1173 K for 8 h.

Figure **5.9** (b) depicts the fluctuation in conductivity as a function of frequency at fixed temperature for all synthesized BGCTO-0.05, BGCTO-0.1, and BGCTO-0.2 sintered ceramic. Two sections were exhibited from the experimental curve in which one is at lower frequency sides and the other is the higher frequency region. The conductivity in the lower frequency region shows little dependence is comparable to dc conductivity (σ_{dc}) while in the higher frequency region, the conductivity is strongly dependent on a frequency which is

equivalent to ac conductivity (σ_{ac}). The following Jonscher's power law conductivity, in general, is given by Equation **5.1**.

$$\sigma(\omega) = \sigma_{dc} + A\omega^{s} \quad (5.1)$$

$$\sigma_{ac} = A\omega^{s}$$

Where s, ω, and A are the frequency exponent parameter, angular frequency, and pre-exponential factor, respectively [**43**]. The value of exponent parameters (s) is obtained from the slope of the curve and measured to be 0.8, 0.88, and 0.89, respectively for BGCTO-0.05, BGCTO-0.1 and BGCTO-0.2 sintered ceramics at room temperature. The value of s calculated from the plot is found to be less than 1 and greater than 0 and its value increases with the increase of doping concentrations of Gd in the BCTO ceramic which is an indication of the hoping behaviour of materials.

AC conductivity [ln σ vs 1000/T (K)] as a function of temperature at a particular frequency (1 kHz) for BGCTO-0.05, BGCTO-0.1, and BGCTO-0.2 sintered ceramics is shown in Figure **5.9** (a). The increment in conductivity with the rise of temperature is observed from the plot of ln σ vs 1000/T. Further, In the lower frequency region, the temperature dependence conductivity was strongly dominant in comparison to the higher frequency which occurs due to the existence of a thermally activated process from the various localized sites in the band gap [**44**]. The activation energy value for Gd doped BCTO ceramic at a particular frequency can be calculated by fitting the thermal plots of Ac conductivity revealed in Figure **5.9** (a) to the general conduction activation mechanism,

$$\sigma = \sigma_0 exp\frac{-E_{cond}}{k_b T} \quad (5.2)$$

Where σ_0 is the pre-exponential term and E_{cond} is the activation energy for conduction. The value of activation energy for BGCTO-0.05, BGCTO-0.1, and BGCTO-0.2 sintered ceramics at 1 kHz frequency is found to be 0.25, 0.235, and 0.210 respectively. It is perceived from the result that the value of E_{cond} decreases with an increase in the doping concentration of Gd in BCTO ceramic. A linear drop in activation energy with compositions causes a rise in charge carriers that improves the conductivity of synthesized ceramics [**45**].

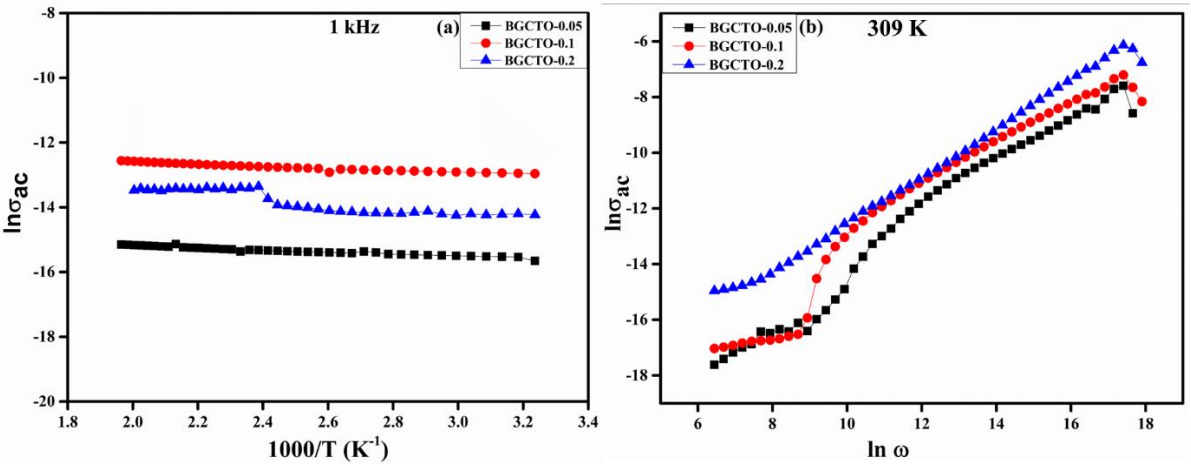

Fig. 5.9 (a) and (b) Variation of conductivity with the inverse of temperature at a few selected frequencies and Frequency dependence of AC conductivity at a few selected temperatures of $Bi_{(2/3)-x}Gd_xCu_3Ti_4O_{12}$ (x = 0.05, 0.10 and 0.20) ceramics sintered at 1173 K for 8 h.

5.4. Conclusion

In the present study, BGCTO-0.05, BGCTO-0.1, and BGCTO-0.2 ceramics were successfully synthesized by semi-wet route using metal nitrate solutions and solid TiO_2. Single-phase formation by sintering at 1173 K was confirmed by XRD. Scanning electron micrographs show the presence of clear grain-grain boundaries and also faceted grain morphology having a grain size in the range of 0.5 μm-1.5 μm. The stoichiometry of synthesized samples was confirmed by EDS studies. The particle size was measured by the TEM analysis. The dielectric constant as well as tangent loss increase with increasing the concentration of Gd^{3+}.

Impedance studies confirmed that ceramics is electrically heterogeneous with semi-conducting grains and insulating grain boundaries. Further, it may be also concluded that frequency dependence AC part of conductivity obeyed Jonscher's power law ($\sigma_{ac} = A\omega^{S}$) and their frequency exponent factor (s) increases with increasing concentrations of Gd^{3+} in BCTO ceramic, following the inverse trends of conductivity provided by the Correlated Barrier Hopping (CBH) mechanism. The conductivity of BGCTO ceramic with temperature supports the Arrhenius law and a linear decrease in the value of E_{cond} with doping concentrations improves the conductivity of synthesized ceramics.

5.5. References

[1] K. D. Mandal, A. K. Rai, D. Kumar, O. Parkash, "Dielectric properties of the $Ca_{1-x}La_xCu_3Ti_{4-x}Co_xO_{12}$ system (x= 0.10, 0.20 and 0.30) synthesized by semi-wet route," Journal of alloys and compounds, **478** (2009) 771-776.

[2] A. K. Rai, K. D. Mandal, D. Kumar, O. Parkash, "Characterization of nickel doped CCTO: $CaCu_{2.9}Ni_{0.1}Ti_4O_{12}$ and $CaCu_3Ti_{3.9}Ni_{0.1}O_{12}$ synthesized by semi-wet route," Journal of alloys and compounds, **491** (2010) 507-512.

[3] D. Huang, W. -L. Li, Z. -F. Liu, Y. -X. Li, C. Ton-That, J. Cheng, W. C. H. Choy, F. C. -C. Ling, "Electron-pinned defect dipoles in (Li, Al) co-doped ZnO ceramics with colossal dielectric permittivity," Journal of materials chemistry A, **8** (2020) 4764-4774.

[4] L. Yang, X. Kong, F. Li, H. Hao, Z. Cheng, H. Liu, J. -F. Li, S. Zhang, "Perovskite lead-free dielectrics for energy storage applications," Progress in Materials Science, **102** (2019) 72-108.

[5] C. Zhao, J. Wu, "Effects of secondary phases on the high-performance colossal permittivity in titanium dioxide ceramics," ACS applied materials & interfaces, **10** (2018) 3680-3688.

[6] W. Dong, W. Hu, T. J. Frankcombe, D. Chen, C. Zhou, Z. Fu, L. Cândido, G. Hai, H. Chen, Y. Li, R. L. Withers, Y. Liu, "Colossal permittivity with ultralow dielectric loss in In+Ta co-doped rutile TiO_2" Journal of materials chemistry A, **5** (2017) 5436-5441.

[7] X. Cheng, Z. Li, J. Wu, "Colossal permittivity in ceramics of TiO_2 Co-doped with niobium and trivalent cation," Journal of Materials Chemistry A, **3** (2015) 5805-5810.

[8] R. Schmidt, M. C. Stennett, N. C. Hyatt, J. Pokorny, J. Prado-Gonjal, M. Li, D. C. Sinclair, "Effects of sintering temperature on the internal barrier layer capacitor (IBLC) structure in $CaCu_3Ti_4O_{12}$ (CCTO) ceramics," Journal of the European Ceramic Society, **32** (2012) 3313-3323.

[9] P. Liang, Y. Li, F. Li, X. Chao, Z. Yang, "Effect of the synthesis route on the phase formation behavior and electric property of $Na_{0.5}Bi_{0.5}Cu_3Ti_4O_{12}$ ceramics," Materials Research Bulletin **52** (2014) 42-49.

[10] A. K. Rai, N. K. Singh, S. -K. Lee, K. D. Mandal, D. Kumar, O. Parkash, "Dielectric properties of iron doped calcium copper titanate, $CaCu_{2.9}Fe_{0.1}Ti_4O_{12}$," Journal of alloys and compounds **509** (2011) 8901-8906.

[11] Y. Q. Tan, J. L. Zhang, W. T. Hao, G. Chen, W. B. Su, C. L. Wang, "Giant dielectric-permittivity property and relevant mechanism of $Bi_{2/3}Cu_3Ti_4O_{12}$ ceramics," Materials Chemistry and Physics, **124** (2010) 1100-1104.

[12] E. A. Patterson, S. Kwon, C. -C. Huang, D. P. Cann,"Effects of ZrO_2 additions on the dielectric properties of $CaCu_3Ti_4O_{12}$," Applied physics letters, **87** (2005).

[13] A. Cho, C. S. Han, M. Kang, W. Choi, J. Lee, J. Jeon, S. Yu, Y. S. Jung, Y. S. Cho, "Direct correlations of grain boundary potentials to chemical states and dielectric properties of doped $CaCu_3Ti_4O_{12}$ thin films," ACS applied materials & interfaces, **10** (2018) 16203-16209.

[14] H. M. Kang, S. -H. Baek, J. H. Song, Y. S. Cho, J. -W. Choi, "Full range dielectric characteristics of calcium copper titanate thin films prepared by continuous composition-spread sputtering," ACS Combinatorial Science, **16** (2014) 478-484.

[15] L. Yang, G. Huang, T. Wang, H. Hao, Y. Tian, "Colossal dielectric permittivity and relevant mechanism of $Bi_{2/3}Cu_3Ti_4O_{12}$ ceramics," Ceramics International, **42** (2016) 9935-9939.

[16] A. K. Rai, K. D. Mandal, D. Kumar, O. Parkash, "Dielectric properties of $CaCu_3Ti_{4-x}Co_xO_{12}$ (x=0.10, 0.20, and 0.30) synthesized by semi-wet route," Materials Chemistry and Physics, **122** (2010) 217-223.

[17] J. Jumpatam, N. Chanlek, P. Thongbai, "Giant dielectric response, electrical properties and nonlinear current-voltage characteristic of Al_2O_3-$CaCu_3Ti_4O_{12}$ nanocomposites," Applied Surface Science, **476** (2019) 623-631.

[18] S. -Y. Chung, I. -D. Kim, S. -J. L. Kang, "Strong nonlinear current–voltage behaviour in perovskite-derivative calcium copper titanate," Nature materials, **3** (2004) 774-778.

[19] P. Thongbai, J. Jumpatam, B. Putasaeng, T. Yamwong, S. Maensiri, "The origin of giant dielectric relaxation and electrical responses of grains and grain boundaries of W-doped $CaCu_3Ti_4O_{12}$ ceramics," Journal of Applied Physics, **112** (2012).

[20] J. Jumpatam, B. Putasaeng, T. Yamwong, P. Thongbai, S. Maensiri, "Effects of Bi^{3+} doping on microstructure and dielectric properties of $CaCu_3Ti_4O_{12}/CaTiO_3$ composite ceramics," Ceramics International, **41** (2015) S498-S503.

[21] J. Liu, C. Duan, W. N. Mei, R. W. Smith, J. R. Hardy, "Dielectric properties and Maxwell-Wagner relaxation of compounds $ACu_3Ti_4O_{12}$ (A= ca, $Bi_{2/3}$, $Y_{2/3}$, $La_{2/3}$)," Journal of applied Physics, **98** (2005).

[22] S. Krohns, P. Lunkenheimer, S. G. Ebbinghaus, A. Loidl, "Colossal dielectric constants in single-crystalline and ceramic $CaCu_3Ti_4O_{12}$ investigated by broadband dielectric spectroscopy," Journal of Applied Physics, **103** (2008).

[23] W. C. Ribeiro, E. Joanni, R. Savu, P. R. Bueno, "Nanoscale effects and polaronic relaxation in $CaCu_3Ti_4O_{12}$ compounds," Solid state communications, **151** (2011) 173-176.

[24] K. Sun, L. -F. Xu, C. Mao, X. Feng, J. -Y. Liang, H.-B. Xiao, R.-L. Wang, D. -W. Shi, C. -P. Yang, "Preferential orientation and relaxation behaviors of $CaCu_3Ti_4O_{12}$ thin films in a low frequency range," Journal of Alloys and Compounds, **704** (2017) 676-682.

[25] K. Barner, X. J. Luo, X. P. Song, C. Hang, S. S. Chen, I. V. Medvedeva, C. P. Yang, "Correlation between the trap state spectra and dielectric behavior of $CaCu_3Ti_4O_{12}$," Journal of Materials Research, **26** (2011) 395-406.

[26] W. Hao, J. Zhang, Y. Tan, W. Su, "Giant dielectric-permittivity phenomena of compositionally and structurally $CaCu_3Ti_4O_{12}$-like oxide ceramics," Journal of the American Ceramic Society, **92** (2009) 2937-2943.

[27] J. Liu, C. -G. Duan, W. -G. Yin, W. N. Mei, R. W. Smith, J.R. Hardy, "Large dielectric constant and maxwell-wagner relaxation in $Bi_{2/3}Cu_3Ti_4O_{12}$," Physical review B, **70** (2004) 144106.

[28] Z. Yang, P. Liang, L. Yang, P. Shi, X. Chao, Z. Yang, "Synthesis, dielectric properties of $Bi_{2/3}Cu_3Ti_4O_{12}$ceramics by the sol–gel method," Journal of Materials Science: Materials in Electronics, **26** (2015) 1959-1968.

[29] P. Gautam, A. Khare, S. Sharma, N. B. Singh, K. D. Mandal, "Characterization of $Bi_{2/3}Cu_3Ti_4O_{12}$ ceramics synthesized by semi-wet route," Progress in Natural Science: Materials International, **26** (2016) 567-571.

[30] V. Kumar, A. Kumar, M. K. Verma, S. Singh, S. Pandey, V. S. Rai, D. Prajapati, T. Das, N. B. Singh, K. D. Mandal, "Investigation of dielectric and electrochemical

behavior of $CaCu_{3-x}Mn_xTi_4O_{12}$ (x=0, 1) ceramic synthesized through semi-wet route," Materials Chemistry and Physics, **245** (2020) 122804.

[31] V. S. Rai, S. Pandey, V. Kumar, M. K. Verma, A. Kumar, S. Singh, D. Prajapati, K. D. Mandal, "Investigation of microstructure and dielectric behavior of $Bi_{2/3}Cu_{3-x}Mg_xTi_4O_{12}$ (x= 0, 0.05, 0.1 and 0.2) ceramics synthesized by semi-wet route," Journal of Materials Science: Materials in Electronics, **32** (2021) 7671-7680.

[32] G. Sreenu, S. Saha, R. N. Bhowmik, J. P. Praveen, D. Das, "Investigation of structural, electrical, and dielectric properties of lead-free $(BiFeO_3)(1-x)-(CaTiO_3)x$ ceramics," Journal of Materials Science: Materials in Electronics, 33 (2022) 24959-24971.

[33] X. Huang, H. Zhang, M. Wei, Y. Lai, J. Li, "Effect of semiconductive grain and microstructure on the dielectric properties of $CaCu_3Ti_4O_{12}$ ceramics with Sr^{2+} doping," Journal of Alloys and Compounds, **708** (2017) 1026-1032.

[34] L. da Conceição, A. M. Silva, N. F. P. Ribeiro, M. M. V. M. Souza, "Combustion synthesis of $La_{0.7}Sr_{0.3}Co_{0.5}Fe_{0.5}O_3$ (LSCF) porous materials for application as cathode in IT-SOFC." Materials Research Bulletin, **46** (2011) 308-314.

[35] X. Zhao, H. Yang, Z. Cui, X. Wang, Z. Yi, "Growth process and CQDs-modified $Bi_4Ti_3O_{12}$ square plates with enhanced photocatalytic performance," Micromachines, **10** (2019) 66.

[36] N. Tian, Y. Zhang, H. Huang, Y. He, Y. Guo, "Influences of Gd substitution on the crystal structure and visible-light-driven photocatalytic performance of Bi_2WO_6," The Journal of Physical Chemistry C, **118** (2014) 15640-15648.

[37] L. Singh, I. W. Kim, B. C. Sin, K. D. Mandal, U. S. Rai, A. Ullah, H. Chung, Y. Lee, "Dielectric studies of a nano-crystalline $CaCu_{2.90}Zn_{0.10}Ti_4O_{12}$ electro-ceramic by one

pot glycine assisted synthesis from inexpensive TiO_2 for energy storage capacitors," RSC Advances, **4** (2014) 52770-52784.

[38] W. Tuichai, S. Danwittayakul, N. Chanlek, M. Takesada, A. Pengpad, P. Srepusharawoot, P. Thongbai, "High-performance giant dielectric properties of Cr^{3+}/Ta^{5+} Co-doped TiO_2 ceramics," ACS omega, **6** (2021) 1901-1910.

[39] V. S. Rai, D. Prajapati, V. Kumar, M. K. Verma, S. Pandey, T. Das, N. B. Singh, K. D. Mandal, "Low temperature synthesis, dielectric and electrical characteristics of $Bi_{2/3}Cu_{3-x}Ni_xTi_4O_{12}$(where x=0.05, 0.1, and 0.2) ceramics for the dielectric and electrical properties," Journal of Materials Science: Materials in Electronics, **33** (2022) 5273-5282.

[40] A. Kumar, S. S. Yadava, P. Gautam, A. Khare, K. D. Mandal, "Magnetic and dielectric studies of barium hexaferrite ($BaFe_{12}O_{19}$) ceramic synthesized by chemical route," Journal of Electroceramics, **42** (2019) 47-56.

[41] S. S. Yadava, L. Singh, S. Sharma, K. D. Mandal, N. B. Singh, "Effect of temperature on the dielectric and ferroelectric properties of a nanocrystalline hexagonal $Ba_4YMn_3O_{1.5-\delta}$ ceramic synthesized by a chemical route," RSC Advances, **6** (2016) 68247-68253.

[42] S. Singh, A. Kumar, S. K. Pandey, V. Kumar, M. K. Verma, A. Gupta, K. D. Mandal, "Synthesis of $Bi_4Ti_3O_{12}$-$BaTiO_3$ nanocomposite, manifesting high dielectric and unique magnetic nature applicable in heterogeneous photocatalytic activity for degradation of Rhodamine B dye," Materials Technology, **36** (2021) 476-491.

[43] L. Singh, U. S. Rai, K. Mandal, B. C. Sin, S.-I. Lee, Y. Lee, "Dielectric, AC-impedance, modulus studies on $0.5BaTiO_3$-$0.5CaCu_3Ti_4O_{12}$ nano-composite ceramic

synthesized by one-pot, glycine-assisted nitrate-gel route," Ceramics International, **40** (2014) 10073-10083.

[44] Y. Slimani, A. Selmi, E. Hannachi, M. A. Almessiere, A. Baykal, I. Ercan, "Impact of ZnO addition on structural, morphological, optical, dielectric and electrical performances of $BaTiO_3$ ceramics," Journal of Materials Science: Materials in Electronics, **30** (2019) 9520-9530.

[45] M. A. Ahmed, M. A. El Hiti, M. K. El Nimr, M. A. Amer, "The ac electrical conductivity for Co-substituted SbNi ferrites," Journal of magnetism and magnetic materials, **152** (1996) 391-395.